

Fabrication of comb-drive actuators for straining nanostructured suspended graphene

M. Goldsche,^{1,2} G. J. Verbiest,¹ T. Khodkov,^{1,2,*} J. Sonntag,^{1,2} N. von den Driesch,² D. Buca,² and C. Stampfer^{1,2}

¹*JARA-FIT and 2nd Institute of Physics, RWTH Aachen University, 52074 Aachen, Germany*

²*Peter Grünberg Institute (PGI-8/9), Forschungszentrum Jülich, 52425 Jülich, Germany*

We report on the fabrication and characterization of an optimized comb-drive actuator design for strain-dependent transport measurements on suspended graphene. We fabricate devices from highly p-doped silicon using deep reactive ion etching with a chromium mask. Crucially, we implement a gold layer to reduce the device resistance from ≈ 51.6 k Ω to ≈ 236 Ω at room temperature in order to allow for strain-dependent transport measurements. The graphene is integrated by mechanically transferring it directly onto the actuator using a polymethylmethacrylate membrane. Importantly, the integrated graphene can be nanostructured afterwards to optimize device functionality. The minimum feature size of the structured suspended graphene is 30 nm, which allows for interesting device concepts such as mechanically-tunable nanoconstrictions. Finally, we characterize the fabricated devices by measuring the Raman spectrum as well as the a mechanical resonance frequency of an integrated graphene sheet for different strain values.

1. INTRODUCTION

Graphene offers unique combinations of electrical and mechanical properties¹, which allows for flexible electronics² as well as high-frequency resonators³⁻⁵, sensors^{6,7}, filters⁸, mixers⁹⁻¹¹ and amplifiers⁹⁻¹¹. The application of strain alters the mechanical properties, e.g. the resonance frequency of suspended graphene devices^{3,4}, but more remarkably also the electronic properties. Strain induces a pseudo-vector similar to that of a real magnetic field¹²⁻¹⁴. Control over strain fields¹⁵ may lead to fully strain engineered devices such as valley-filters¹² as well as piezoelectric¹⁶ and superconducting¹⁷ devices. However, the experimental realization of such devices has proven to be a major challenge. In commonly used methods, such as pulling on suspended flakes with a bottom-electrostatic gate or bending a flexible substrate, the obtained strain fields are intrinsically linked to either the electronic tuning of the charge carrier density^{3,4,18-22} or to the properties of the substrate^{19,20,23-25}. Here we report on the fabrication and characterization of surface micromachined silicon-based comb-drive (CD) actuators to strain suspended graphene. The devices are low-temperature compatible and allow to decouple the obtained strain fields from the electronic tuning of the charge carrier density and from the properties of the substrate. In addition, we implement a gold layer on the CD actuators to reduce the contact resistance to the suspended graphene in order to enable transport measurements. Finally, we introduce a technique to pattern suspended graphene with a minimum feature size of 30 nm after its mechanical transfer onto the CD actuators to optimize device functionality and to enable mechanically-tunable suspended nanoconstriction devices and potentially suspended quantum dots.

A CD actuator consist of two interdigitated combs (see figure 1(a)) of which one is fixed to a substrate and one that is held suspended by springs. By applying a po-

tential difference between the fingers of the combs, an electrostatic force arises due to their capacitive coupling resulting in a displacement of the suspended comb. The important design parameters for CD actuators are the overlap area of the fingers²⁶, the shape of the fingers^{27,28} and the distance between them²⁶. To maximize the capacitive coupling, a high overlap area and small finger separation is desired. Consequently, the comb structures have high aspect ratios: the thickness of the fingers is much larger than their separation.

CD actuators are usually surface micromachined from polycrystalline silicon²⁹⁻³¹ that is grown on a sacrificial layer, e.g silicon oxide. The comb structures are patterned via optical lithography³² and then carved into the polycrystalline silicon by reactive ion etching (RIE)³³. Finally, one of the combs is released from the substrate by removing the sacrificial silicon oxide layer with (buffered) hydrofluoric acid (HF)^{34,35} or hydrofluoric vapor³⁶. Standard optical lithography limits the minimal feature size, e.g. the finger width or the distance between the fingers, to around 0.5 μm . Concomitantly, the low capacitive coupling requires high voltages to reach the maximum displacement of the CD actuator, e.g. the design in Ref. 37 needs 400 V. When reducing the minimal feature size into the nanometer regime with electron beam lithography, the scallops resulting from the RIE process on the vertical surface of the CD fingers become increasingly important and decreases the reliability of the actuator³⁸. Along the same line, polycrystalline silicon actuators typically show a lower reliability than monocrystalline silicon. We therefore fabricate our low-temperature compatible CD actuators based on highly p-doped monocrystalline silicon using electron beam lithography.

The paper is organized as follows. We first introduce our actuator design (Sect. 2). This is then followed by a detailed description of the fabrication process in Sect. 3. This includes a subsection for the substrate preparation, the deep reactive ion etch process, the integration of a

thin Au film, the transfer of graphene, the patterning of suspended graphene, and the release of the actuator from the substrate. Finally, we characterize the fabricated actuators in Sect. 4 by measuring the induced strain in the graphene with the help of spatially-resolved scanning confocal Raman spectroscopy^{15,39,40} and by measuring its tunable mechanical resonance frequency with an amplitude modulated down-mixing technique⁴¹.

2. DESIGN

To ensure low operating voltages, we reduce the minimal feature size down to 60 nm. A schematic illustration of our actuator design is depicted in figures 1(a-b). Our CD design differs from commonly used CD designs^{42,43} (see e.g. figure 1(c)) at two points. We change the direction of motion (indicated with the orange arrows in figure 1) in comparison to common actuators by designing the interdigitated fingers on purpose asymmetric (figure 1(b)), i.e. unequal distances between the fingers. In figure 1(c), we show the standard symmetric placement of the fingers and resulting direction of motion for comparison. To prevent the suspended comb from moving in the direction indicated by the orange arrow in figure 1(c), we apply interdigitated fingers to both sides of the suspended comb.

We compared the performance of our CD design in figure 1(a) with the symmetric design in figure 1(c) using a finite element simulation⁴⁴. In these simulations, the finger overlap area and total number of fingers were for both CD designs the same. We computed the actuator displacement δ as a function of applied actuator potential V_a . Figure 1(d) shows that our CD designs reaches up to 5 times more displacement than the symmetric design for the same V_a . In addition, we increased the length of the actuator along the direction of motion to decrease the rotation resulting from a non-perfectly transferred graphene flake (see Sect. 3.5). Note that the maximum displacement of the actuator is for the asymmetric design lower than for the symmetric design. However, the maximum displacement translates to over 4% of strain for a graphene flake with a typical suspended length of 2 μm , which exceeds the experimentally observed breaking strength in doubly clamped suspended graphene¹⁵. As such the travel range is not the limiting factor, especially considering that the design of the actuator is easily adjustable to allow for higher maximum displacements. Similar to common actuators, the suspended comb body consist of a grated structure to ensure release from the substrate, and has integrated stoppers (see gray arrows in figure 1(a)) to limit its displacement and thereby prevent an electrical connection between the interdigitated fingers. Finally, we point out the possibility to integrate an electrostatic gate in the design underneath the transfer area (dashed red boxes in figures 1(a) and 1(c)) to additionally tune the charge carrier density in the graphene.

3. FABRICATION

3.1. Substrate preparation

We start with a commercially available (100) silicon-on-insulator (SOI) wafer (G8P-214-01, UnibondTM wafers, Soitec) with a top layer of 200 nm and a buried oxide thickness of 1 μm . First, we use dry thermal oxidation at 1050 $^\circ\text{C}$ to obtain a 50 nm thick silicon oxide (SiO_2) layer. Second, we remove the SiO_2 layer with HF chemistry. By repeating these steps three times, we are left with a SOI wafer with a top Si layer of 50 nm. Third, we use an industry-compatible reduced-pressure chemical vapor deposition (CVD) system for the epitaxial growth of a 2 μm thick highly p-doped silicon layer on top of the SOI wafers. Prior growth, the native oxide was removed ex-situ using HF vapor chemistry. A subsequent in-situ hydrogen bake ensures a contaminant-free, pristine silicon surface. For the epitaxial growth, we use disilane (Si_2H_6) and diborane (B_2H_6) as a precursor at a temperature of 850 $^\circ\text{C}$ to ensure elevated growth rates and a high boron dopant concentration of about $1.5 \times 10^{19} \text{ cm}^{-3}$. This yields a sheet resistance of $\approx 43.7 \Omega/\square$ and ensures full functionality of the device at cryogenic temperatures ($T \approx 10 \text{ mK}$)⁴¹.

3.2. Deep reactive ion etching process

The 2 μm thick p-doped silicon layer in combination with a minimal feature size of the fingers of 200 nm is demanding on the deep reactive ion etching (DRIE) that is widely used in surface machining and consequently for structuring CD actuators. The minimal feature size requires electron beam lithography, as it is below the resolution of our standard optical lithography. Compared to standard optical lithography, electron beam lithography offers the flexibility and precision to rapidly prototype and optimize the actuator design. However, electron beam resists such as polymethylmethacrylate (PMMA) are generally not suitable for patterning CD actuators, as their DRIE etch rates are comparable to that of the substrate^{45,46}. We circumvent this via the deposition of a chromium (Cr) hard mask, which has a negligible edge rate in reactive ion etching processes⁴⁷. Chromium is a standard mask in III-V semiconductor processing which is known to have a small line edge roughness⁴⁷ and is easily removed with a mixture of perchloric acid (HClO_4), and ceric ammoniumnitrate $(\text{NH}_4)_2[\text{Ce}(\text{NO}_3)_6]$. The Cr mask is patterned in a resist stack of copolymer (AR617.04, 250 nm) and PMMA (AR679.04, 270 nm) using electron beam lithography. Most importantly, the Cr mask allows for the implementation of standard DRIE processes. Nevertheless, the large aspect ratio of 10:1 is problematic, as any deviation from the ideal etching behavior will directly affect the device functionality, relying on the rather homogeneous capacitance between the individual fingers. Note that the issue is even more prob-

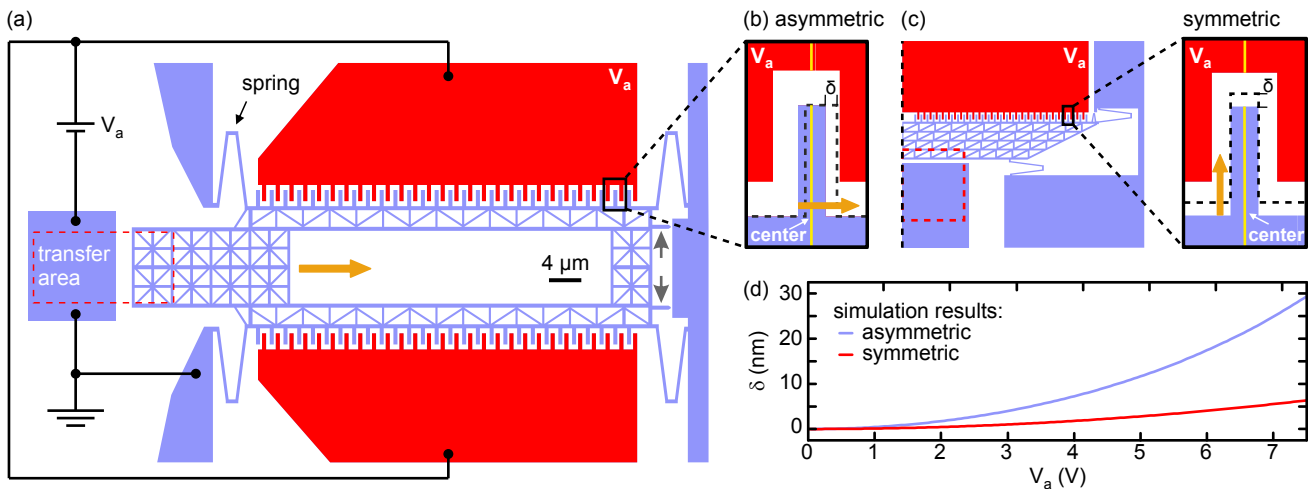


Figure 1. (a) Schematic illustration of the actuator design considered in this work. The gray arrows indicate the stoppers (see text). We place the fingers on purpose asymmetric (b) with respect to the center, which is in contrast with the common symmetric placement (c) of the fingers. Note that we only show half of the symmetric design in the left panel in (c) as indicated by the vertical black dashed line. In (a) and (c), the red box indicates the area where we transfer the graphene and the orange arrows indicate the direction of motion. (d) A finite element simulation shows that design (a) has up to 5 times larger displacement δ than design (c) for the same actuator potential V_a , finger overlap area, and total number of fingers.

lematic for the stoppers (gray arrows in figure 1a), as their separation from the fixed anchor is just 60 nm and thus requires an aspect ratio of 33:1.

Figure 2(a) shows a schematic illustration of a standard reactive ion etch with a mixture of SF_6/O_2 without inductively coupled plasma (ICP). As the tilted scanning electron microscope (SEM) images in figures 2(b-c) show, this results in a notching structure underneath the Cr mask. The notching structure is caused by a significant sideways etching rate of the silicon due to sidewall charging^{48,49}. Therefore, we use a Bosch DRIE process⁵⁰. A schematic illustration of this process is depicted in figure 2(d). We use C_4F_8 with a radio frequency (RF) power of 24 W and an ICP power of 300 W for 10 s to generate a passivation layer. This is followed by SF_6 with a RF power of 12 W and an ICP power of 200 W for 4 s to isotropically etch the substrate. We repeat these steps 20 times to etch 2 μm deep. This Bosch DRIE process does not generate a notching structure underneath the Cr mask (see the tilted SEM image in figure 2(e)). However, as the tilted SEM figure 2(f) shows, this Bosch DRIE process generates scallops and thus results in a higher sidewall roughness. As this has been identified as one of the main sources of the reduced fracture strength³⁸, we implemented an additional etching step with a mixture of SF_6/O_2 that has a RF power of 60 W for 60 s after the final SF_6 step (see illustration in figure 2(g)). As figure 2(h-i) shows, we do not see evidence that the additional etching with SF_6/O_2 causes a notching structure underneath the Cr mask (see figures 2(a-c)). However, the additional etching step dramatically reduces the scallop depth and thus the sidewall roughness to below 5 nm (see inset in figure 2(h)). The width of the fingers of the

structure in figure 2(h) is only ≈ 130 nm smaller than the Cr mask, which corresponds to an average undercut of ≈ 65 nm. Finally, we point out that the width of the fingers in the devices reported in Ref. 15 is only ≈ 30 nm smaller than the Cr mask, which corresponds to an average undercut of ≈ 15 nm.

3.3. Integration of thin Au film

To study charge carrier transport through graphene, the high resistance of the actuator (≈ 50 k Ω at room temperature (red data points in figure 3) and ≈ 1 M Ω at 2.2 K⁴¹) poses a major challenge. The high device resistance diminishes any resistance change of the graphene in two-terminal transport measurements. We solve this problem by depositing a thin metal layer on the actuator before the deposition of the Cr mask needed for the actuator fabrication (see above). It is not possible to do this after the actuator fabrication due to the large thickness of the fingers (2 μm) compared to the required electron beam resist thickness (≈ 500 nm). We use gold (Au) for the thin metal layer, as it is known to have a low contact resistance to graphene⁵¹ and is unaffected by the HF acid required for the release of the actuator from the substrate. However, Au has a low adhesion to the highly p-doped silicon. Therefore, we use an additional thin metal layer of Cr or Tantalum (Ta) for enhancing the adhesion of the Au layer.

We implement the thin Au film as depicted in figure 4(a). A HF dip is performed to remove the natural oxide on the substrate. This ensures a clean interface and thus increases the adhesion of the metal to the

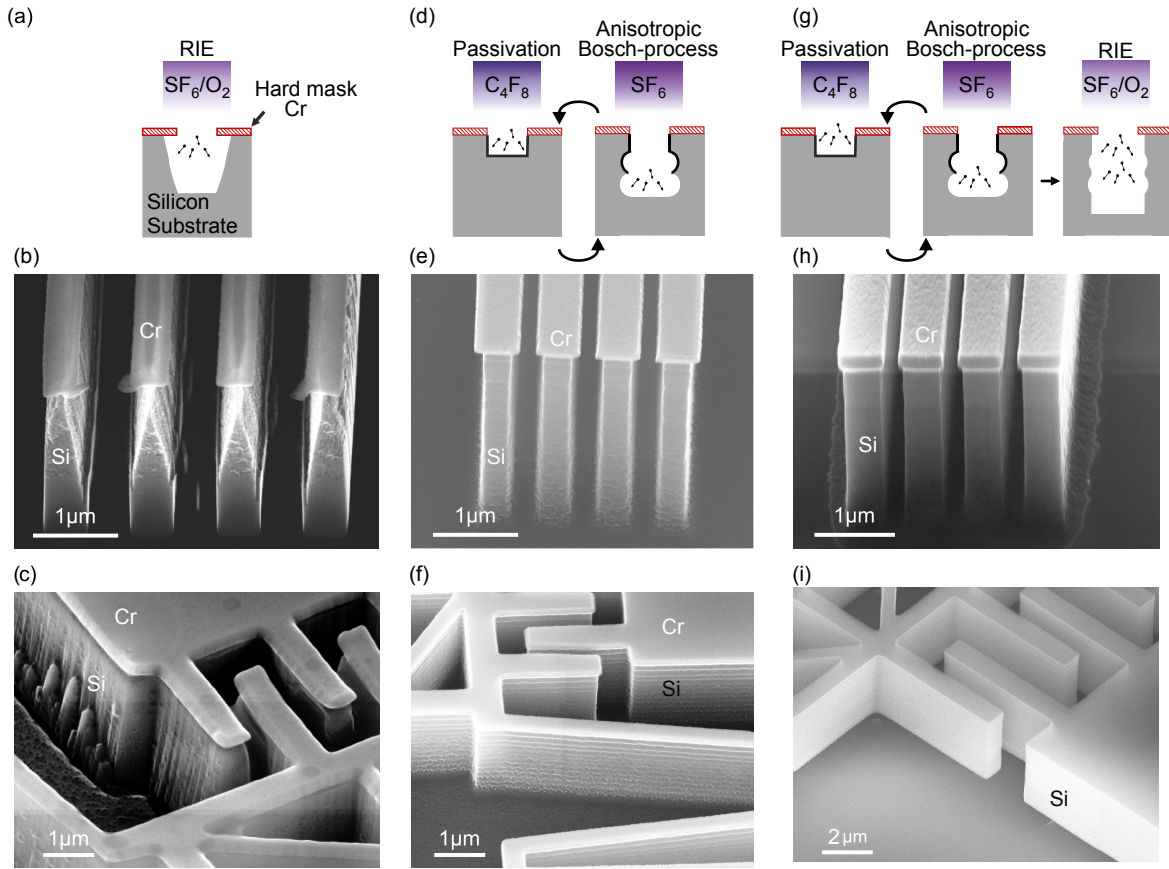


Figure 2. Schematic illustrations and scanning electron microscope images of different etch processes used to reach a depth of $2\ \mu\text{m}$: (a-c) a standard RIE process using SF_6/O_2 without ICP generates an unacceptably large undercut underneath the Cr mask, (d-f) a Bosch DRIE process achieves aspect ratios of up to 10:1, but also generates significantly large scallops, (g-i) a standard optimized RIE process using an additional SF_6/O_2 etch step after the DRIE process depicted in panel (d) reduces the scallops to below $5\ \text{nm}$ (see inset in panel (h)), which is required for optimal CD actuator performance.

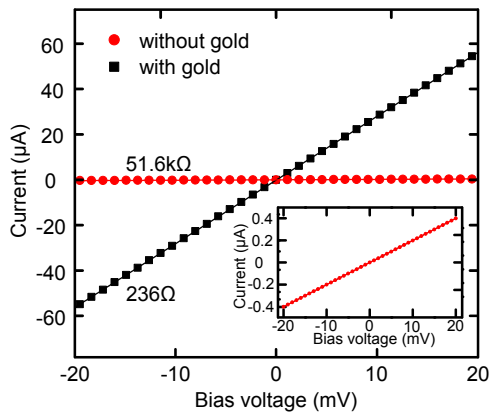


Figure 3. The current through the actuator as a function of applied bias voltage for a device at room temperature without gold (red) and with gold layer (black). The inset provides a zoom-in of the measurement without the gold layer. The gold lowers the resistance through the device from $51.6\ \text{k}\Omega$ to $236\ \Omega$.

substrate. Then an electron beam lithography step is used to deposit Ta ($7\ \text{nm}$) and Au ($30\ \text{nm}$) on an area that is slightly smaller than that of the Cr mask used for the CD actuator fabrication (see figure 4(b)). The Cr mask thus fully encapsulates the deposited metal (see figure 4(c)) and thereby prevents any contamination of the DRIE chamber during etching. Sometimes, we first only partially etch the highly p-doped silicon and then deposit an additional Cr layer for the fabrication of an electrostatic gate before etching completely through. The method outlined here results in a thin layer of metal (see figure 4(d)-(e)) over the entire actuator as shown in figure 4(f), and results in a reduction of the device resistance to $236\ \Omega$ (black data points in figure 3).

3.4. Integration of graphene

To integrate graphene onto the CD actuator, we use a method based on the one reported by Dean et al.⁵². We spin coat a silicon substrate with a $\approx 300\ \text{nm}$ thick layer of polyvinyl alcohol (PVA) and a $\approx 330\ \text{nm}$ thick layer of

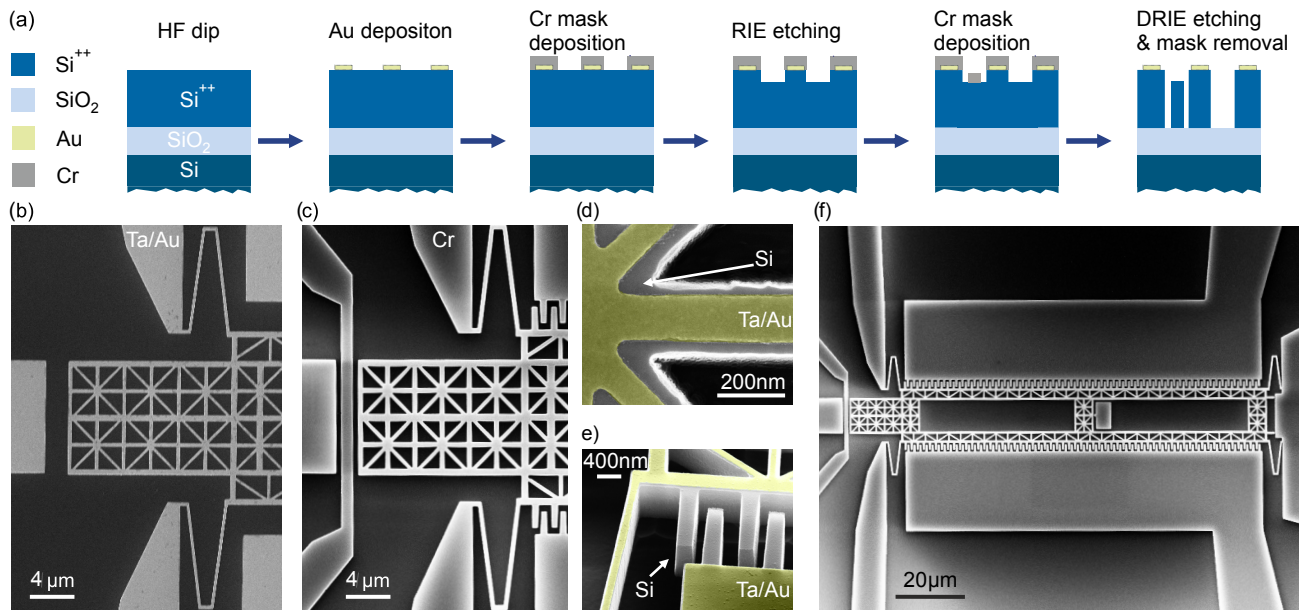


Figure 4. (a) A schematic illustration of the process steps taken to integrate a metal onto the actuator and to fabricate an electrostatic gate underneath the transfer region. The scanning electron microscope images (b-f) show different steps of the fabrication process: (b) After HF dip and Au deposition, (c) after Cr mask deposition, (d) and (e) show a top and side view of the implemented metal after DRIE and Cr mask removal. (f) Top view of the final device.

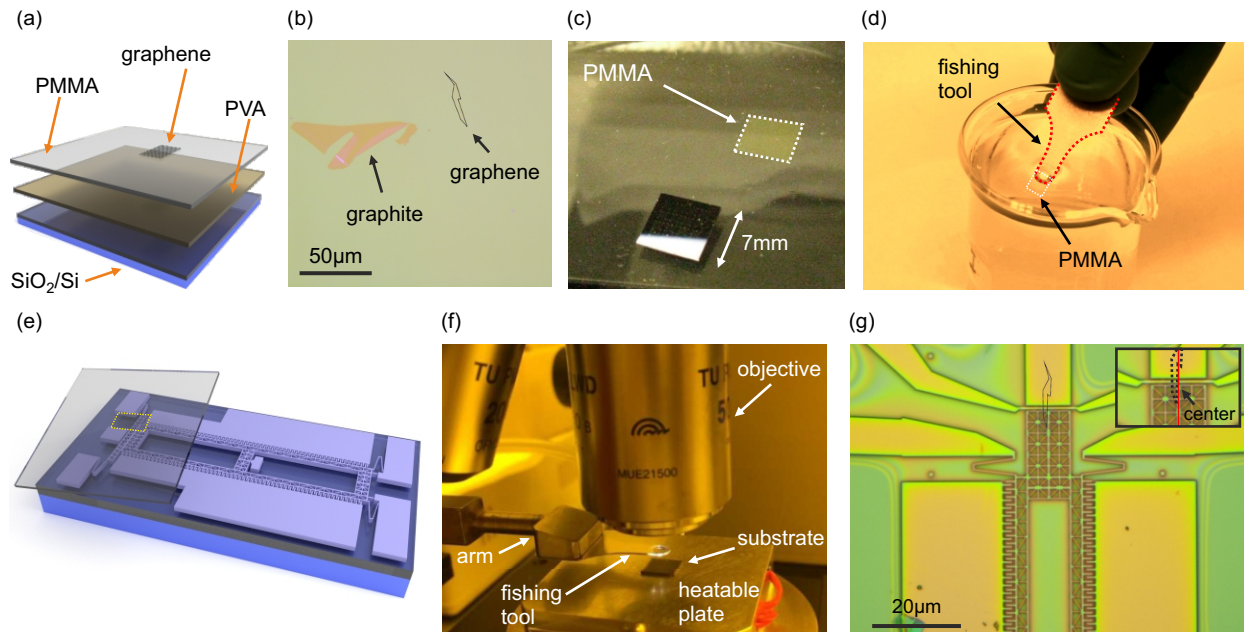


Figure 5. Integration of graphene: (a) Mechanical exfoliation of a graphene onto a PVA/PMMA stack. (b) Identification of individual flakes with an optical microscope, (c) dissolving the PVA with DI water before picking it up with a fishing tool (d). (e) Schematic illustration of the transfer of the PMMA membrane with the graphene flake onto the actuator using the in setup (f). Panel (g) shows an optical image of the transferred graphene flake. The close-up depicts the misalignment ($\approx 3 \mu\text{m}$) between the graphene flake (see dashed line) and the center of the actuator (red line).

PMMA (see figure 5(a)). These thicknesses are selected to optimize the contrast of individual graphene flakes in optical microscopy⁵³. Then, we exfoliate graphene onto the prepared substrate. Using an optical microscope, we identify an isolated graphene flake with typical dimen-

sions of $2 \mu\text{m}$ by $10 \mu\text{m}$ (see figure 5(b)). After the identification of a suitable graphene flake, we submerge the substrate into deionized (DI) water to dissolve the PVA. Note that the graphene does not get in contact with the water during this step. Figure 5(c) shows that

the PMMA with an exfoliated graphene flake floats on top of the DI water. This PMMA membrane is fished out of the DI water with an open circle that has a slightly smaller diameter than the membrane (see figure 5(d)). To transfer the PMMA membrane onto the actuator (see figures 5(e-f)), we align the graphene flake with the transfer area of the actuator and make sure that they are in the same focus depth. Then we use a nitrogen flow to press the PMMA membrane into contact with the actuator before heating up the actuator to 120 °C to ensure good mechanical contact. Finally, we lift up, i.e. mechanically remove, the fishing device leaving the graphene and the PMMA layer attached to the CD actuator (see figure 5(g)).

3.5. Patterning suspended graphene

The integrated graphene flake is usually not exactly in the center of the transfer area of the actuator. This misalignment, i.e. the distance to the center of the transfer area, can be up to 5 μm , which affects the operation of the actuator. The graphene flake acts as an additional spring k_g connected to the actuator. Consequently, the force of the actuator on the transfer area will be unevenly distributed (see inset figure 6). This results in a rotation of the actuator.

We quantify the rotation of the actuator for the designs depicted in figure 1(a) and figure 1(c) by extracting the

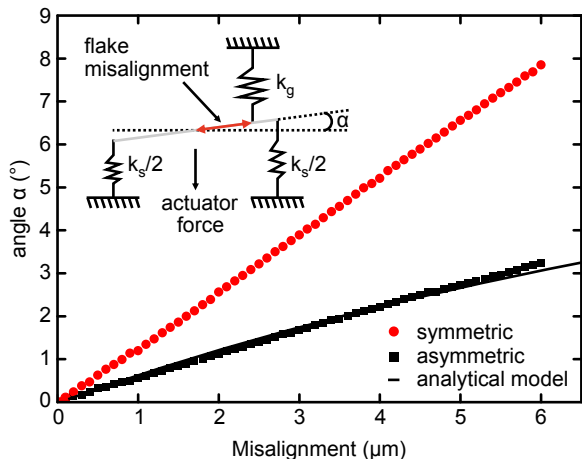


Figure 6. Finite element simulation of the rotation angle α when applying strain to a graphene flake as a function of the misalignment as defined by the dashed red line in the inset. The result for a fixed actuator force of 6.75 μN indicates that α for the design with the asymmetrically spaced fingers depicted in Fig. 1b is up to 3 times smaller and therefore approaches the ideal actuator behavior with $\alpha = 0^\circ$. The simulation for the asymmetrically spaced fingers is in good agreement with the analytical solution for α when modeling the graphene as a spring $k_g = 540 \text{ N/m}$ connected to a single point on the CD actuator with spring constant $k_s = 6.5 \text{ N/m}$, as depicted in the inset.

rotation angle α as a function of the misalignment for a fixed force of 6.75 μN from a finite element simulation with COMSOL⁴⁴. In the simulation, the spring constant k_g of the graphene was 540 N/m and the spring constant k_s of the CD actuator was 6.5 N/m. The spring constant $k_g = Y_{2D}W/L$ was chosen to approximate the spring constant of a typically transferred graphene flake with a width W of $\approx 3 \mu\text{m}$ and a suspended length L of 2 μm . Here, $Y_{2D} = 340 \text{ N/m}$ is the two-dimensional Young's modulus of graphene⁵⁴. The result, shown in figure 6, illustrates that our CD design has up to 3 times less rotation compared to the symmetric actuator design. In addition, the simulation for the design depicted in figure 1(a) is in good agreement with the analytical model for α (inset figure 6). Nevertheless, the rotation angle α generates a non-negligible shear strain in the integrated graphene sheet.

A viable method to circumvent the misalignment problem is to transfer graphene flakes that are comparable in size to the transfer area of the CD actuator (see figure 1(a)). We then pattern the simultaneously transferred PMMA membrane with an electron dose of $\approx 120 \mu\text{C}/\text{cm}^2$ at 20 kV. After development of the PMMA membrane, we structure the suspended graphene with reactive ion etching using SF_6 with a RF power of 60 W for 6 s and thereby regain control over the position and geometry of the graphene flake. Figure 7(a) shows an optical image of a transferred PMMA layer with exfoliated graphene. Note the fringes indicated by the black arrows in figure 7(a), which indicate the height change of the PMMA membrane when going from the CD actuator to the substrate. By using reactive ion etching, we are able to structure the graphene such that it is well aligned with the center of the transfer area (see SEM image in figure 7(b)). A second example is depicted in figures 7(c-d), in which we even reduced the graphene width to 500 nm. The described patterning process gives us control over the geometry of suspended graphene flakes and is not only applicable to our CD devices. To show this, we prepared a substrate with a 0.3 μm thick highly p-doped silicon layer (see Sect. 3.1) and used DRIE to structure a 1 μm wide and 350 nm deep trench in it (see Sect. 3.2). After transferring a PMMA layer with exfoliated graphene over the trench (see figure 7(e)), we structured several suspended nanoconstrictions (see tilted SEM image in figure 7(f)). Figure 7(g) shows a zoom-in of the narrowest (30 nm) constriction we made. By this technique, we are thus able to build suspended structures with a minimum feature size up to 30 nm. This promising approach allows for suspended nanoconstriction devices (see figures 7(e-g)) and potentially quantum dot devices⁵⁵. Finally, we point out that this method of structuring a transferred graphene flake is generally applicable to other suspended graphene devices such as resonators as well as to two-dimensional materials in general.

After structuring the suspended graphene flake, we have to clamp it to the actuator. Hereby, we prevent the removal of the graphene flake during the release of

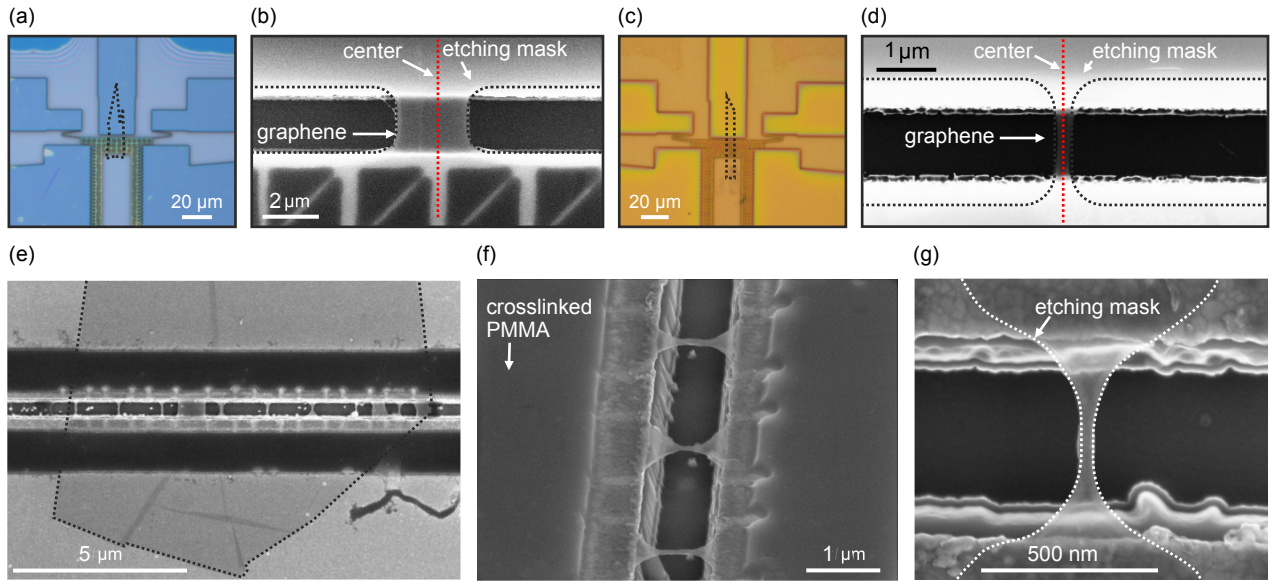


Figure 7. (a-d) Structuring the graphene flakes after transfer onto an actuator: (a) and (c) Optical image of the flake prior structuring. (b) and (d) Scanning electron microscope image after structuring. Panels (b) and (d) show that the structured flake is almost perfectly aligned with the center of the actuator. The designed width of the graphene flakes was 2 μm and 0.5 μm in panels (b) and (d), respectively. Note the fringes indicated by the black arrows in panel (a), which indicate the height change of the simultaneously transferred PMMA membrane. (e-f) Structuring a suspended graphene flake over a 1 μm wide trench: scanning electron microscope images of (e) the initial flake, (f) suspended nanoconstrictions, (g) and the narrowest constriction (30 nm) achieved with this technique.

the device from the substrate. In addition, strong clamping of the graphene to the actuator is required to induce strain in the graphene as well as to prevent slipping of the graphene. Ideally, the graphene flake ruptures before the clamping does. We found that clamping the graphene by cross-linking the remaining PMMA after structuring that is on top of both the actuator and the graphene sheet with an electron dose of 10.000 $\mu\text{C}/\text{cm}^2$ fulfills all the mentioned requirements¹⁵.

3.6. Release from the substrate

After the transfer and patterning of the graphene, we dissolve the non-crosslinked PMMA in acetone and transfer the actuator into DI water. We finally release the combs that are connected to a grated structure by submerging the entire device into a 10% HF acid solution. The grated structure ensures that the HF solution reaches all the SiO_2 underneath. Consequently, this comb is suspended and freely movable whereas the other comb remains fixed to the substrate. The HF solution has an etch rate of ≈ 1 nm/s, which sets the total etching time to ≈ 15 minutes. After etching, we flush the device with DI water for 10 min. Then, we shortly flush the device with isopropanol. As the surface tension is strong enough to pull the actuator down to the substrate, we finally use a critical point dryer (CPD) to remove the liquids from the actuator.

4. CHARACTERIZATION

To show the functionality of our CD actuators with integrated graphene, we present measurements performed on two different devices. In the first set of measurements, depicted in figure 8, we performed confocal Raman spectroscopy on a controllably strained graphene flake. We use linearly polarized laser light ($\lambda \approx 532$ nm) with a power of 0.5 mW and a spot size of ≈ 500 nm. The scattered light is detected by a CCD spectrometer with a grating of 1200 lines/mm. With Raman spectroscopy one probes optical phonons via the inelastic scattering of light. Note that the frequency of optical phonons depends on the crystal lattice and therefore on the applied strain. The Raman spectrum of graphene contains a peak at $\omega_G \sim 1580$ cm^{-1} and at $\omega_{2D} \sim 2665$ cm^{-1} (see figure 8(a)), which are the so-called G- and 2D-mode peaks, respectively. As the electrostatic force of the CD actuator on the graphene flake is proportional to V_a^2 , the induced strain in the graphene sheet should show the same dependence. As figure 8(b) shows, we indeed observe a parabolic tuning V_a^2 of ω_{2D} . The G-peak frequency shows similar behavior (not shown). Combining the measured ω_G and ω_{2D} for different V_a into figure 8(c), we observe that the data points follow roughly a straight line with a slope of 2.67. We attribute the relatively large spread to spatial inhomogeneities in the doping of the graphene sheet within the laser spot size⁵⁶. Experiments reported in the literature show that this slope is characteristic for strain induced frequency shifts^{15,23,24,56}. By using the re-

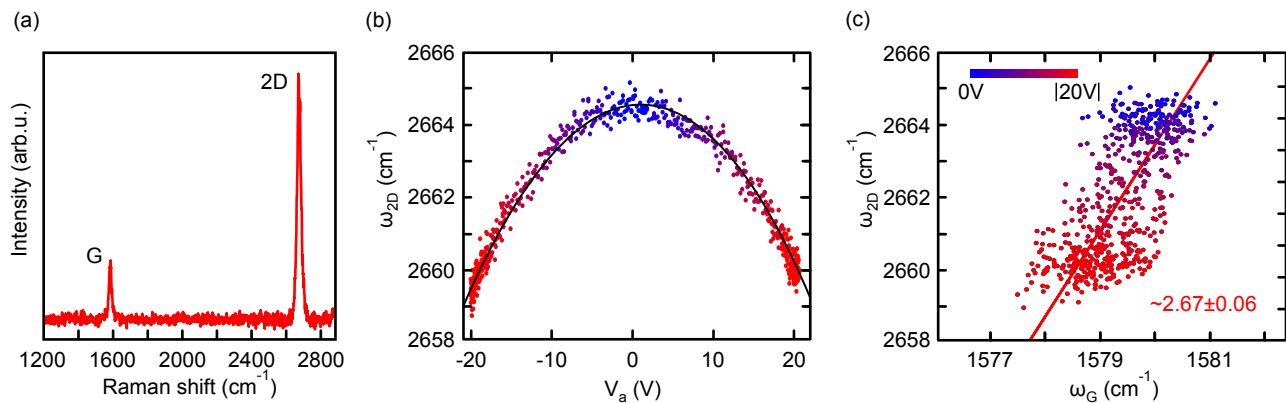


Figure 8. (a) A typical Raman spectrum of graphene obtained after transfer onto the CD actuator. (b) shift of the Raman active 2D-mode as a function of applied actuator potential. The parabolic fit (black line) is in agreement with the electrostatic force $\sim V_a^2$. (c) the relative shift of the Raman active 2D- and G-mode have an overall linear correlation with a slope of 2.67, which is a clear indication that the actuator induces strain into the graphene sheet. We attribute the relatively large spread to spatial inhomogeneities in the doping of the graphene sheet within the laser spot size⁵⁶.

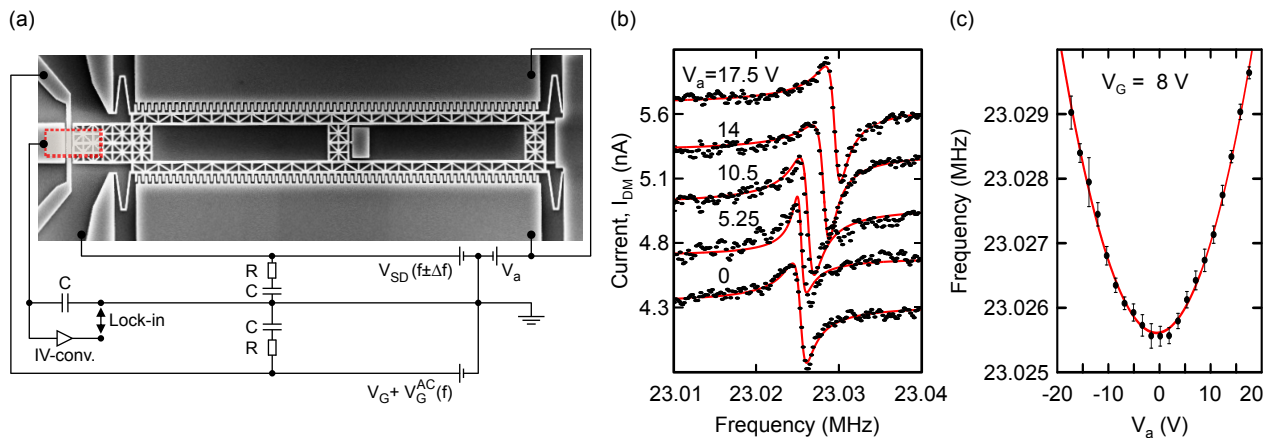


Figure 9. (a) A SEM image of the device with its electrical connections. An AC signal ($V_{SD}(f \pm \Delta f)$) at frequency $f \pm \Delta f$ biases the graphene resonator (red dashed box) while a sum of DC and AC voltages ($V_G + V_G^{AC}(f)$) are applied to the gate underneath. The down-mixed current I_{DM} at frequency Δf is measured with an IV-converter and a lock-in amplifier. A DC voltage V_a controls the actuator. The capacitors $C = 100$ nF and resistors $R = 50 \Omega$ are chosen for impedance matching and decoupling any high frequency signals. (b) The measured down-mixing current I_{DM} as a function of the actuation frequency f for different V_a shows a resonance around 23.0254 MHz. The curves are offset for clarity. The red lines represent fits to a non-zero phase Lorentzian^{3,57}. (c) The extracted resonance frequency as a function of applied V_a . The parabolic fit (red line) is in agreement with the electrostatic force $\sim V_a^2$ that increases the strain in the resonator.

ported value of $-83 \text{ cm}^{-1}/\%$ for the frequency shift of ω_{2D} per unit of applied uniaxial strain²³, we find a maximum strain value of 0.06%. Note that the spring constant of the graphene is much stiffer than that of the actuator such that 20 V is needed to elongate the graphene by only 1.2 nm (c.f. Fig. 1). A detailed discussion on the effect of the spring constants in relation to the measured Raman shifts can be found in Ref. 15. So far, we reached a maximum strain value of 1.2% in a controllable and reproducible fashion with the CD actuator presented in this work¹⁵. This shows that the actuator is strong enough to induce a strain value above 1% in suspended graphene flakes.

In a second test experiment, we measure a mechanical resonance frequency of a graphene flake integrated onto

an CD actuator operating at 2.2 K using an amplitude modulated down-mixing scheme (see figure 9(a))^{3,41}. In this scheme, we apply a DC voltage V_G as well as an AC voltage V_G^{AC} at frequency f to the electrostatic gate below the graphene in order to tune the charge carrier density and to mechanically actuate it. In addition, a small modulation voltage $V_{SD} = 10$ mV at frequency $f \pm \Delta f$ is applied across the graphene membrane to generate a current I_{DM} at frequency Δf , which is amplified with an IV-converter and measured with an UHF lock-in amplifier from Zürich Instruments. Figure 9(b) shows the unprocessed I_{DM} around the resonance peak for different V_a and the corresponding fit with a non-zero phase Lorentzian (red lines)^{3,57}. The extracted resonance frequency and quality factor are 23.0254 MHz and 15.220,

respectively. These numbers are comparable with similar experiments performed on graphene resonators reported in the literature^{3,58}. In analogy to the Raman measurement, the electrostatic force generated by applying a voltage V_a to the actuator strains the graphene sheet. The induced strain and thus tension in the graphene sheet naturally results in an increase of the resonance frequency, as depicted in figure 9(c). Note that the applied V_{SD} also results in a constant Joule heating of 7 nW, which is independent from V_a and therefore cannot explain the observed change in resonance frequency as observed in Ref. 59. The observed parabolic tuning of the resonance frequency (red line in figure 9(c)) is in agreement with the applied electrostatic force. Moreover, this measurement proves the functionality of the CD actuators at cryogenic temperatures.

5. CONCLUSION AND OUTLOOK

We integrated suspended graphene on CD actuators to perform strain-dependent measurements. We presented an optimized CD actuator design and described in detail the fabrication process. We presented a DRIE process to fabricate CD actuators with a scallop depth below 5 nm and a process to implement a gold layer on top of the Si actuator. In particular, the actuator resistance at room temperature reduces from 51.6 k Ω to 236 Ω after implementing the gold. This enables sensitive electrical measurements as a function of strain on integrated

suspended graphene. The functionality of the fabricated actuators was shown by measuring the Raman spectrum and the mechanical resonance frequency of an integrated graphene sheet as a function of induced strain.

Moreover, we introduced a method to structure suspended graphene flakes. When applying this method to integrated graphene flakes on actuators, ideal device functionality can be realized. The minimum feature size achievable with this method is up to 30 nm, which enables device concepts such as suspended quantum dots and nanoconstrictions. This method is also applicable to other suspended graphene devices such as resonators.

The methods for integrating graphene and structuring suspended graphene presented in this work are generally applicable to other two-dimensional materials. Therefore, this work provides a toolbox for strain dependent (transport) measurements in two-dimensional materials, which is not only interesting from the fundamental point of view but also for the development of novel device concepts for applications in the fields of sensors and transducers.

6. ACKNOWLEDGEMENT

The authors thank S. Trellenkamp and B. Hermanns for the support and discussions concerning the actuator fabrication. We acknowledge support from the Helmholtz Nano Facility (HNF)⁶⁰ and funding from the ERC (GA-Nr. 280140).

-
- * Current address: ICFO, Barcelona, Spain
- ¹ Novoselov K S, Geim A K, Morozov S V, Jiang D, Zhang Y, Dubonos S, Grigorieva I V and Firsov A A 2004 *Science* **306** 666–669
 - ² Kim S J, Choi K, Lee B, Kim Y and Hong B H 2015 *Annu. Rev. Mater. Res.* **45** 63–84
 - ³ Chen C, Rosenblatt S, Bolotin K I, Kalb W, Kim P, Kymissis I, Stormer H L, Heinz T F and Hone J 2009 *Nat. Nanotech.* **4** 861–867
 - ⁴ Bunch J S, Van Der Zande A M, Verbridge S S, Frank I W, Tanenbaum D M, Parpia J M, Craighead H G and McEuen P L 2007 *Science* **315** 490–493
 - ⁵ Eichler A, Moser J, Chaste J, Zdrojek M, Wilson-Rae I and Bachtold A 2011 *Nat. Nanotech.* **6** 339–342
 - ⁶ Bogue R 2014 *Sensor Rev.* **34** 233–238
 - ⁷ Verbiest G J, Kirchhof J N, Goldsche M, Khodkov T, Sonntag J and Stampfer C 2018 arxiv.org/abs/1802.01906
 - ⁸ Jiang Y, Biswas P and Fortner J D 2016 *Environ. Sci.: Water Res. Technol.* **2** 915–922
 - ⁹ Zhou Q and Zettl A 2013 *Appl. Phys. Lett.* **102** 223109
 - ¹⁰ Zhou Q, Jinglin Z, Onishi S, Crommie M and Zettl A 2015 *Proc. Natl. Acad. Sci.* **112** 8942
 - ¹¹ Heath M S and Horsell D W 2017 *Sci. Rep.* **7** 1363
 - ¹² Pereira V M and Castro Neto A H 2009 *Phys. Rev. Lett.* **103** 046801
 - ¹³ Guinea F, Katsnelson M and Geim A 2010 *Nat. Phys.* **6**, 30–33
 - ¹⁴ Verbiest G J, Brinker S and Stampfer C 2015 *Phys. Rev. B* **92** 075417
 - ¹⁵ Goldsche M, Sonntag J, Khodkov T, Verbiest G J, Reichardt S, Neumann C, Ouaj T, von den Driesch N, Buca D and Stampfer C 2018 *Nano Lett.* **18** 1707–1713
 - ¹⁶ Smith A D, Niklaus F, Paussa A, Schröder S, Fischer A C, Sterner M, Wagner S, Vaziri S, Forsberg F, Esseni D, Östling M and Lemme M C 2016 *ACS Nano* **10** 9879
 - ¹⁷ Uchoa B and Barlas Y 2013 *Phys. Rev. Lett.* **111** 046604
 - ¹⁸ Song X, Oksanen M, Sillanpää M A, Craighead H, Parpia J and Hakonen P J 2011 *Nano Lett.* **12** 198–202
 - ¹⁹ Zhang H, Huang J-W, Jr J V, Myhro K, Maldonado M, Tran D D, Zhao Z, Wang F, Lee Y, Liu G, Bao W and Lau C N 2014 *Carbon* **69** 336–341
 - ²⁰ Guan F, Kumaravadevel P, Averin D V and Du X 2015 *Appl. Phys. Lett.* **107** 193102
 - ²¹ Nicholl R J, Conley H J, Lavrik N V, Vlassioug I, Puzyrev Y S, Sreenivas V P, Pantelides S T and Bolotin K I 2015 *Nat. Commun.* **6** 8789
 - ²² Bao W, Myhro K, Zhao Z, Chen Z, Jang W, Jing L, Miao F, Zhang H, Dames C and Lau C N 2012 *Nano Lett.* **12** 5470
 - ²³ Mohiuddin T M G, Lombardo A, Nair R R, Bonetti A, Savini G, Jalil R, Bonini N, Basko D M, Galiotis C and Marzari N 2009 *Phys. Rev. B* **79** 205433
 - ²⁴ Yoon D, Son Y W and Cheong H 2011 *Phys. Rev. Lett.* **106** 155502

- ²⁵ Huang M, Yan H, Heinz T F and Hone J 2010 *Nano Lett.* **10** 4074–4079
- ²⁶ Legtenberg R, Groeneveld A W and Elwenspoek M 1996 *J. Micromech. Microeng* **6** 320
- ²⁷ Jensen B D, Mutlu S, Miller S, Kurabayashi K and Allen J J 2003 *J. Microelectromech. Syst.* **12** 373–383 ISSN 1057-7157
- ²⁸ Goldsche M, Khodkov K, Kaienburg P, Neumann C, Stampfer C, Trellenkamp S and Mussler G 2014 Low-temperature compatible electrostatic comb-drive actuators with integrated graphene *Proceedings of the 9th IEEE International Conference on Nano/Micro Engineered and Molecular Systems* pp 251–255
- ²⁹ Jack W J 2001 *Smart Mater. Struct.* **10** 1115
- ³⁰ Sasaki M, Briand D, Noell W and de Rooij N 2003 Vertical comb drive actuator constructed by buckled bridges in soi-mems 2003 *IEEE/LEOS International Conference on Optical MEMS (Cat. No.03EX682)* pp 89–90
- ³¹ 2005 *PolyMUMPs Design Handbook* (MEMSCAP)
- ³² Lorenz H, Despont M, Fahrni N, Brugger J, Vettiger P and Renaud P 1998 *Sens Actuators A Phys* **64** 33 – 39 ISSN 0924-4247
- ³³ Rangelow I W 2003 *J. Vac. Sci. Technol. A* **21** 1550–1562
- ³⁴ Proksche H, Nagorsen G and Ross D 1992 *J. Electrochem. Soc.* **139** 521–524
- ³⁵ Spierings G A C M 1993 *J. Mater. Sci.* **28** 6261–6273
- ³⁶ Helms C R and Deal B E 1992 *J. Vac. Sci. Technol. A* **10** 806–811
- ³⁷ Li P, Sasaki T, Pan L and Hane K 2012 *Opt. Express* **20** 627–634
- ³⁸ Gaither M S, Gates R S, Kirkpatrick R, Cook R F and DelRio F W 2013 *J. Microelectromech. Syst.* **22** 589–602 ISSN 1057-7157
- ³⁹ Graf D, Molitor F, Ensslin K, Stampfer C, Jungen A, Hierold C and Wirtz L 2007 *Nano Lett.* **7**, 238–242
- ⁴⁰ Neumann C, Reichardt S, Venezuela P, Drögeler M, Banzerus L, Schmitz M, Watanabe K, Taniguchi T, Mauri F, Beschoten B and Stampfer C (2015) *Nat. Commun.* **6**, 8429
- ⁴¹ Verbiest G, Xu D, Goldsche M, Khodkov T, Barzanjeh S, Von den Driesch N, Buca D and Stampfer C 2016 *Appl. Phys. Lett.* **109** 143507
- ⁴² Tang W C, Nguyen T C H and Howe, R T 1989 *Sensors and actuators* **20** 25–32
- ⁴³ Xie H and Fedder G K 2002 *Sensors and Actuators A: Physical* **95** 212–221
- ⁴⁴ www.comsol.com
- ⁴⁵ Chinn J D, Adesida I, Wolf E D and Tiberio R C 1981 *J. Vac. Sci. Technol. A* **19** 1418–1422
- ⁴⁶ Wüst R W, Strasser P, Robin F, Erni D and Jäckel H 2005 *J. Vac. Sci. Technol. B* **23** 3197–3201
- ⁴⁷ Shearn M, Sun X, David Henry M, Yariv A and Scherer A 2010 *Semiconductor Technologies (InTech)*
- ⁴⁸ Chen F F and Chang J P 2012 *Springer Science & Business Media* 187–191
- ⁴⁹ Welch C 2011 *Oxford Instruments Plasma Technology*
- ⁵⁰ Liu Z, Wu Y, Harteneck B and Olynick D 2013 *Nanotechnology* **24** 015305
- ⁵¹ Gahoi A, Wagner S, Bablich A, Kataria S, Passi V and Lemme M C 2016 *Solid State Electron.* **125** 234–239
- ⁵² Dean C R, Young A F, Meric I, Lee C, Wang L, Sorgenfrei S, Watanabe K, Taniguchi T, Kim P and Shepard K L 2010 *Nat. Nanotech.* **5** 722–726
- ⁵³ Casiraghi C, Hartschuh A, Lidorikis E, Qian H, Harutyunyan H, Gokus T, Novoselov K S and Ferrari A C 2007 *Nano Lett.* **7** 2711–2717
- ⁵⁴ Lee C, Wei X, Kysar J W and Hone J 2008 *Science* **321** 385–388
- ⁵⁵ Terrés B, Chizhova L A, Libisch F, Peiro J, Jörger D, Engels S, Girschik A, Watanabe K, Taniguchi T, Rotkin S V, Burgdörfer J and Stampfer C 2016 *Nat. Commun.* **7** 11528
- ⁵⁶ Lee J E, Ahn G, Shim J, Lee Y S and Ryu S 2012 *Nat. Commun* **3** 1024
- ⁵⁷ Zande A M v d, Barton R A, Alden J S, Ruiz-Vargas C S, Whitney W S, Pham P H Q, Park J, Parpia J M, Craighead H G and McEuen P L 2010 *Nano Lett.* **10** 4869–4873
- ⁵⁸ Chen C, Lee S, Deshpande V V, Lee G H, Lekas M, Shepard K and Hone J 2013 *Nat. Nanotech.* **8** 923–927
- ⁵⁹ Ye F, Lee J and Feng P X-L 2018 *Nano Lett.* **18** 1678–1685
- ⁶⁰ Research Center Jülich GmbH. (2017). HNF - Helmholtz Nano Facility, *Journal of large-scale research facilities*, **3**, A112 (2017).